Journal of Alloys and Compounds 509 (2011) 9821–9825

Contents lists available at ScienceDirect

Journal of Alloys and Compounds

journal homepage: www.elsevier.com/locate/jallcom

Hydrothermal synthesis of cubic α-Fe_2O_3 microparticles using glycine: Surface characterization, reaction mechanism and electrochemical activity

Chun-Yang Yin[a,*], Manickam Minakshi[a], David E. Ralph[a], Zhong-Tao Jiang[b], Zonghan Xie[c], Hua Guo[c]

[a] School of Chemical and Mathematical Sciences, Murdoch University, Murdoch, 6150 WA, Australia
[b] School of Engineering and Energy, Murdoch University, Murdoch, 6150 WA, Australia
[c] School of Engineering, Edith Cowan University, Joondalup, WA, 6027, Australia

ARTICLE INFO

Article history:
Received 4 July 2011
Received in revised form 10 August 2011
Accepted 10 August 2011
Available online 19 August 2011

Keywords:
Energy storage materials
Oxide materials
Crystal growth
α-Fe_2O_3 microparticles
Hydrothermal synthesis

ABSTRACT

Cubic α-Fe_2O_3 (hematite) microparticles (side lengths = 0.3–1.3 μm) have been synthesized using glycine and ferric chloride via a simple one-step hydrothermal reaction. Their morphological, mineralogical and surface properties have been determined using scanning electron microscopy (SEM), atomic force microscopy (AFM), X-ray diffractometry (XRD) and X-ray photoelectron spectroscopy (XPS). XRD analysis indicated that the synthesized α-Fe_2O_3 microparticles were minerallogically pure. An increase in hydrothermal reaction duration from 10 to 24 h increased the atomic percentages of α-Fe_2O_3 on the surface of the microparticles by almost 8%. The mechanism concerning reactions of species to produce this microparticles precipitate was elucidated based on thermodynamics and ionic equilibrium aspects. In the electrochemical analysis, the synthesized α-Fe_2O_3 microparticles (as cathode material) exhibit an approximate charge capacity of 160 mAh/g and excellent coulombic efficiency of 94%.

1. Introduction

Iron oxide–hydroxides compounds are ubiquitous in nature with a myriad of uses in the industrial and medical sectors. Iron oxides, in particular, exist in various natural forms, namely, magnetite (Fe_3O_4), maghemite (γ-Fe_2O_3) and hematite (α-Fe_2O_3). In the age of nanotechnology, researchers have managed to manipulate numerous synthesis conditions to produce iron oxides with micro- or nano- dimensions that afford enhanced electrical, magnetic and chemical characteristics. Synthesis of α-Fe_2O_3 micro- and nanoparticles has been widespread due to their high stability and excellent semiconducting properties [1,2]. Previously synthesized α-Fe_2O_3 micro/nanoparticles include single-crystal dendritic micro-pines [3], nanotubes [4], nanorings [5], rod-like nanocrystals [6], micro-nano-octahedrons [7], star-like nanoparticles [8], microspheres [9,10], nanodiscs [11]) and plate-like particles [12] for magnetic [3,8,12], gas sensor [4,5], battery [4,9,11] and catalytic [7] applications.

In this study, a facile one-step hydrothermal reaction method using glycine has been used to synthesize α-Fe_2O_3 microparticles and their morphological, mineralogical and surface properties have been determined. Generally, hydrothermal synthesis involves reaction in an autoclave at temperatures higher than 100 °C using single or multiple precursors. Hydrothermal reaction has been used in this study for the synthesis process due to its ease of operation and relatively low temperature requirement. This method of producing microparticles is useful and may afford advantages over nano-sized Fe_2O_3 particles in niche applications such as medical biochemistry [13] and applications requiring ease of particles dispersion [14]. A feasibility study involving use of the particles as electrochemical cathode materials has also been conducted to assess its applicability in the field of energy storage.

2. Experimental

2.1. Synthesis via hydrothermal reaction

$FeCl_3 \cdot 6H_2O$ (Fluka, >98%) and glycine (Chem-Supply, 99.5%) were mixed in a beaker to create a solution of 0.1 M Fe^{3+}, 0.25 M glycine with a total volume of 35 mL. The solution was then transferred to a Teflon-lined stainless steel vessel (Model 4744, PARR Instrument Company). The vessel was tightly sealed and heated to 160 °C for a specific reaction time in an oven before allowed to cool to room temperature. Measurements of pH before and after the hydrothermal reaction were conducted using a pH meter equipped with Metrohm Unitrode electrode while total iron concentrations in solution were determined using atomic absorption spectrometry (GBC 933AA). At the conclusion of the experiment the maroon-colored precipitate was washed repeatedly with deionized water as well as absolute ethanol and centrifuged for 5 min prior to drying in a vacuum dessicator for 24 h. The two samples are denoted as F10 and F24 for hydrothermal reaction times of 10 and 24 h, respectively.

* Corresponding author. Tel.: +61 4 3140 9216; fax: +61 8 9360 6452.
E-mail addresses: c.yin@murdoch.edu.au, yinyang@streamyx.com (C.-Y. Yin).

0925-8388/$ – see front matter © 2011 Elsevier B.V. All rights reserved.
doi:10.1016/j.jallcom.2011.08.048

2.2. Characterization

The surface morphology of the hydrothermal products was examined using a PHILLIPS XL 20 scanning electron microscopy (SEM) system linked with energy dispersive X-ray analysis. Surface topographic images of the microparticles were obtained using a commercial atomic force microscopy (AFM) (Ntegra Prima, NT-MDT Co., Moscow, Russia) in semi-conduct mode. The microparticles were fixed on adhesive tape before AFM scans were conducted. The probe used for the imaging contained a tetrahedral tip with a height of 14–16 μm and a typical curvature radius of 6 nm. The tip was mounted on a rectangular single crystal silicon (N-type, antimony doped) cantilever with a thickness of 2 μm, a resonant frequency of 140–390 kHz and a force constant of 3.1–37.6 N/m. X-ray diffractometry (XRD) spectra were collected using a GBC EMMA diffractometer operating at 2θ step size of 0.01°.

The atomic percentages and surface bonding structures of hydrothermal products were probed by X-ray photoelectron spectroscopy (XPS) (Kratos Axis Ultra XPS spectrometer, Manchester, UK) with Mg Kα radiation ($h\nu$ = 1253.6 eV). The powder samples were mounted, using double-sided Cu sticky tape, horizontally on the holder and normal to the electrostatic lens. The vacuum pressure of the analyser chamber was better than 10^{-9} Torr. The voltage and emission current of X-ray source were held at 12 kV and 12 mA, respectively. Initial survey scan used pass energy of 80 eV. To ensure high resolution and good sensitivity for the features of interests (i.e. Fe 2p, C1s and O1s), pass energy of 10 eV was used. XPS spectra energy scale was calibrated using Cu 2p (932.67 eV), Ag 3d (368.27 eV), C1s (284.6 eV; hydrocarbon: C–H) and Au 4f (83.98 eV). The electrostatic lens mode and analyser entrance of XPS instrument were selected using the Hybrid and Slot mode (Iris = 0.6 and Aperture = 49), respectively. Charge neutralization was employed during the XPS measurements. The CASA XPS (V.2.3.15) software was utilized for quantification analysis with Shirley background subtraction.

2.3. Electrochemical activity

The potential use of the synthesized α-Fe_2O_3 microparticles as cathode material for battery applications was assessed. An electrochemical cell was used which comprised the α-Fe_2O_3 microparticles as cathode and zinc (99.9%, Advent Research Materials) as anode. The cathode comprised 75 wt% α-Fe_2O_3 microparticles, 15 wt% acetylene black as conductive powder and 10 wt% poly (vinylidene difluoride) (PVDF, Sigma–Aldrich) as binder uniformly mixed in a mortar and pestle and pressed to form a disk-like pellet. The pellet was 10 mm in diameter and 0.3 mm thickness. A filter paper (Whatman filters 12) was used as the separator. The electrolyte was a saturated solution of LiOH containing 1 mol/L zinc sulphate ($ZnSO_4$) with pH 10.5. The cathode material was reduced/oxidized galvanostatically at 0.2 mA/cm^2 using an eight-channel battery analyzer (Shenzhen Neware Technology Company, China) operated by a battery testing system (BTS). The cut-off discharge and charge voltages were +0.25 and +1 V, respectively. All electrochemical measurements were carried out at ambient temperature.

3. Results and discussion

3.1. Morphology of Fe_2O_3 microparticles

Fig. 1 shows the SEM micrographs illustrating the α-Fe_2O_3 microparticles cubic morphology. The side lengths of the particles are in the range 0.3–1.3 μm. The cubic α-Fe_2O_3 microparticles produced in this study are morphologically similar to the hematite microcubes synthesized by Su et al. [15] using ferric chloride and ammonium acetate (CH_3COONH_4). They suggest that in early reaction stage, rod-like β-FeOOH particles form and gradually evolve to a flower-like structure through self-assembly which ultimately develop into cubic structure. They demonstrate that cubic α-Fe_2O_3 particles first appear at 10 h of reaction time and there is no further change in their morphology at 24 h. This explains the reason why increasing the hydrothermal reaction time from 10 to 24 h in our study did not alter the shape and size of the microparticles. Fig. 2 shows the AFM images of F10 and F24, which illustrate a rather smooth textural surface.

Fig. 3 shows the XRD patterns of the α-Fe_2O_3 microparticles. The identification of these patterns (JCPDS-89-2810/89-0599) clearly indicates both samples are purely crystalline α-Fe_2O_3 microparticles. The crystalline system is rhomhohedral with space group R3c(167) (a = 5.04 and c = 13.75) while no other oxidation states can be detected. The peaks intensities in the XRD spectra for

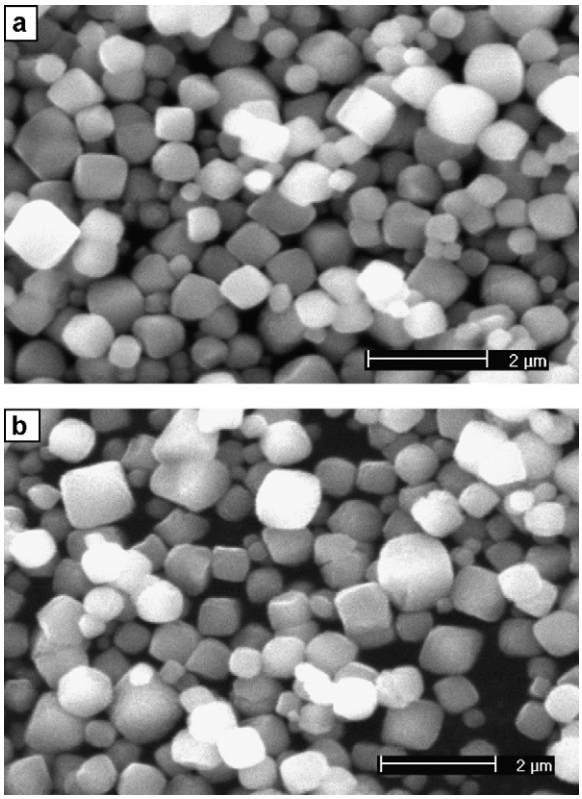

Fig. 1. SEM micrographs of (a) F10, and (b) F24.

F10 and F24 are dissimilar because there is a difference in the orientation of crystalline structure. The increasing peak intensities of (1 1 0), (1 1 6) and (2 1 4) indicate that α-Fe_2O_3 crystals are more inclined to these orientations for the hydrothermal reaction time from 10 to 24 h. The absence of peak broadening (i.e. sharp peaks) indicates high crystallinity of the α-Fe_2O_3 phase, though XRD analysis is not able to detect marginal amorphous phase on the surface of the particles. No other peaks associated with other compounds (impurities) are observed; this indicates that the microparticles are highly pure (mineralogically). It is interesting to note that the hydrothermal reaction time does not have a significant effect on their overall mineralogical characteristics since all prominent peaks are almost identical for both reaction times.

3.2. XPS analysis

Fig. 4 shows the XPS spectra of F10 and F24 with peak-fitting of the C1s, O1s and Fe 2p envelopes. Essentially, there is no qualitative difference between F10 and F24. For both samples, the deconvolution of C1s consists of three carbon components, i.e., (1) C–H, C–C; (2) Fe–C; and (3) C=O, in the order of decreasing atomic percentages. The presence of organic carbon is often detected during XPS analysis of samples, which have not been exposed to reduce carbon directly. The carbon nuclei detected in these samples could have arisen from adsorption of glycine or glycine derivatives or from contamination. The deconvolution of O1s photoelectron spectrum also consists of three components, i.e., (1) Fe_2O_3, (2) Fe(OH), FeO(OH); and (3) C=O, OH, H_2O, in the order of decreasing atomic percentages. It is notable that increasing hydrothermal reaction to 24 h increases the atomic percentages of Fe_2O_3 by almost 8% which implies that prolonging the reaction time enables formation of more Fe_2O_3 compounds from intermediates Fe(OH) and FeO(OH), thereby increasing the Fe_2O_3 concentration on the surface

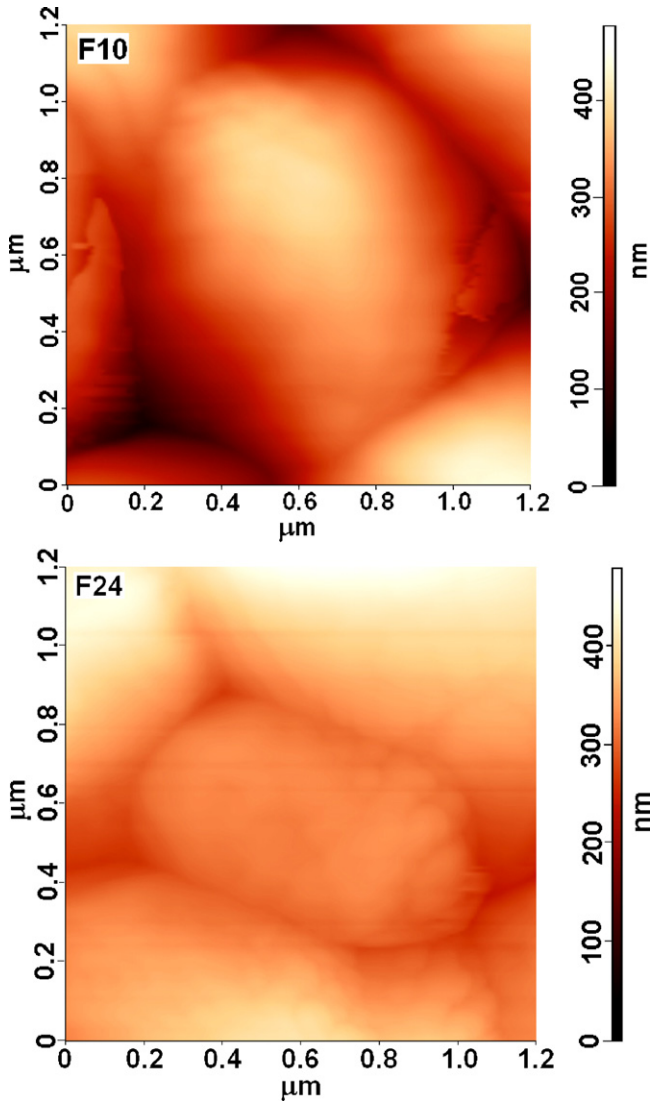

Fig. 2. AFM images of F10 and F24.

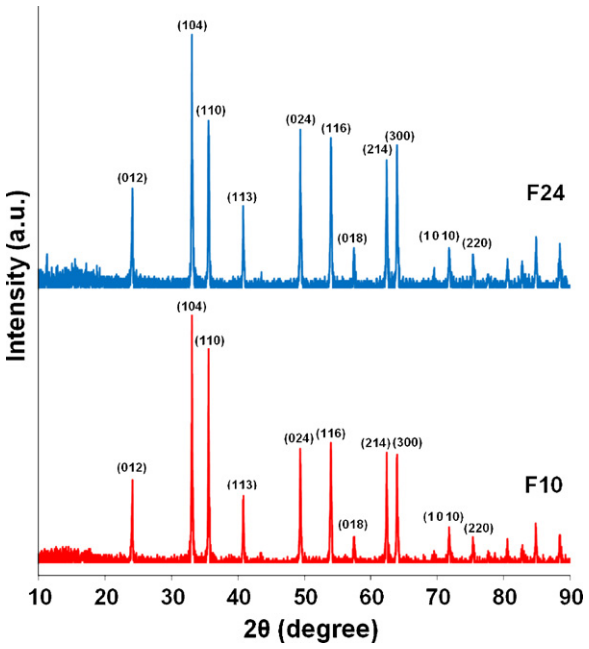

Fig. 3. XRD patterns of (a) F10, and (b) F24.

of the microparticles. The formation of Fe_2O_3 had been previously explained by Li et al. [16] and Singh et al. [17] in which hematite was produced via a two-step phase transformation process from $Fe(OH)_3$ to α-FeOOH and ultimately to α-Fe_2O_3. There are marginal changes in atomic percentages for C1s bonding components since it is expected that the hydrocarbon components in glycine are comparatively unreactive at this condition. Another interesting observation is that only α-Fe_2O_3 is detected in the XRD analysis while the other abovementioned chemical states of elements are detected in XPS analysis. This suggests that only α-Fe_2O_3 is highly crystalline while the other components are amorphous.

3.3. Reaction mechanism

The initial condition in the solution before hydrothermal reaction was a 2.5 molar ratio of glycine (gly) to ferric (Fe^{3+}) ions with a pH of 2.2. The gly and Fe^{3+} species interact strongly in solution forming ferric-glycinate complexes that effectively lower the activity (a) of Fe^{+3} to very low levels. Considering only reaction 1 (Eq. (1)) with log (K_1) = 10.36 [18] and the initial molar ratio of glycine to ferric ions of 2.5, the estimated activity of Fe^{+3} is 3×10^{-11}. This value is too low to exceed the solubility product of $Fe(OH)_3$ (K_2) at pH 2.2 (activity for OH^-, $a_{OH^-} = 10^{-11.8}$) (see Eq. (2)).

$$\begin{aligned} &Fe^{+3} + gly^- \rightleftarrows Fe(gly)^{+2} \\ &K_1 = 10^{10.36} = a_{(Fegly)+2)}/(a_{(Fe+3)\times a(gly-)}) \\ &\Delta_1 H^\circ = -52 \text{ kcal} \end{aligned} \quad (1)$$

$$\begin{aligned} &Fe^{+3} + 3OH^- \rightleftarrows Fe(OH)_3 \\ &K_2 = 1028.44 = a_{(FeOH)3))}/(a_{(Fe+3)\times a(OH-)^3}) \\ &\Delta_2 H^\circ = -22.8 \text{ kcal} \end{aligned} \quad (2)$$

Reaction (1) is however, strongly exothermic and after the chamber is sealed, the temperature increase favors the left side of reaction (1), increasing a_{Fe+3}. It can be predicted from the classic van't Hoff equation (Eq. (3)) that $K_1 = 1$ when the temperature reaches approximately 65 °C (337 K).

$$\log\left(\frac{K_{T2}}{K_{T1}}\right) = \left(\frac{-\Delta_1 H^\circ}{R}\right)[(1/T_2) - (1/T_1)] \quad (3)$$

Reaction (2) is less strongly affected by the temperature rise so at some point the quotient of reaction (2) will exceed K_2 and precipitation of $Fe(OH)_3$ should commence. The pH will certainly become more acidic as the precipitation of $Fe(OH)_3$(s) effectively releases 3 protons for each Fe precipitated, more than can be buffered by the total amount of glycine present. However, given the relative sizes of $\Delta_1 H^\circ$ and $\Delta_2 H^\circ$, along with the relative values of K_1 and K_2, it is expected that once a particular temperature is reached, the system 'buffers' the activity of Fe^{+3} at a relatively constant level high enough to exceed K_2 as the solid $Fe(OH)_3$ phase forms. After the experiment the solution pH values were 0.95 and 0.93 in the F10 and F24 samples, respectively. Residual iron concentrations were approximately 60 mg/L in both experiments showing that more than 99% of the initial iron was converted to the Fe_2O_3 phase.

It has been proposed that some relatively strong bases, propan-1,2-diamine for example, adsorb preferentially to all α-Fe_2O_3 crystal faces except for the (0 0 1) face leading to crystal growth in one direction only [16]. The morphology of the solid phase created in these experiments shows no suggestion of anisotropy in the deposition of iron on particular crystal faces and it was assumed that glycine, or its oxidation products, are not sufficiently basic to

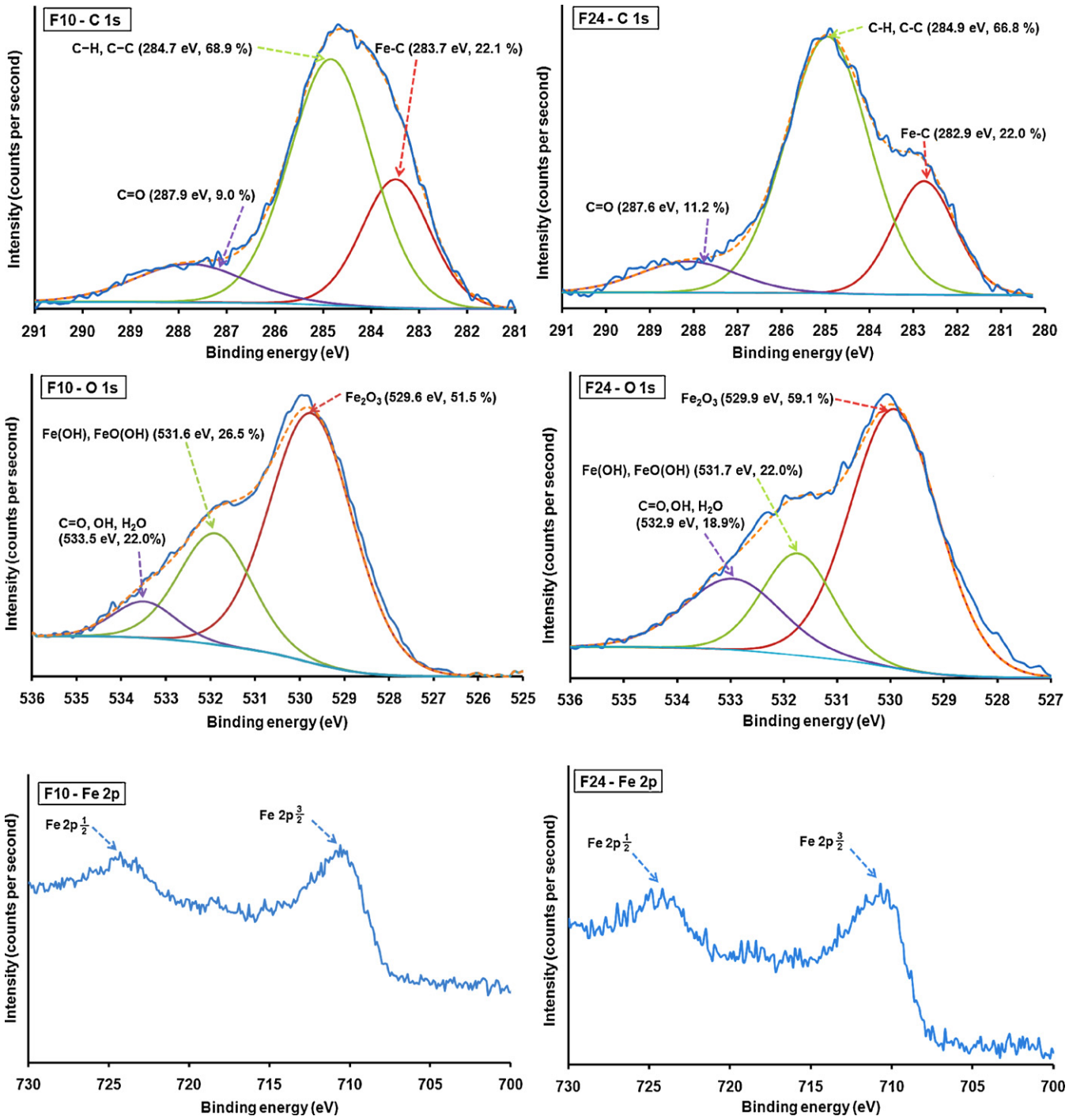

Fig. 4. XPS spectra of F10 and F24. Dashed lines correspond to fit envelopes while wavy lines correspond to raw data curves.

adsorb strongly enough to provide barriers to growth on any of the hematite crystal faces.

3.4. Electrochemical activity

It is well-known that intercalation of lithium or other alkali metal ions into vacant sites of α-Fe_2O_3 compound can be achieved electrochemically using non-aqueous electrolytes [19,20]. However, reports of the formation of lithium intercalation compounds occurring in aqueous media are relatively more limited [21,22]. It has been recently demonstrated that lithium insertion or intercalation can occur in the cathode material of a cell when lithium ions are present in an aqueous electrolyte [23] and thus, such setup is extended for this study. To the best of our knowledge, this is the first time that the electrochemical characteristics of α-Fe_2O_3 compound using aqueous LiOH solution are reported.

The electrochemical activity of the synthesized α-Fe_2O_3 phase was determined by imposing a constant current, producing reduction processes to occur at the α-Fe_2O_3 phase, until the necessary voltage was less than +0.25 V. The direction of the imposed current was then reversed, imposing oxidation processes on the charged 'α-Fe_2O_3–Li' phase, and maintained until the necessary voltage

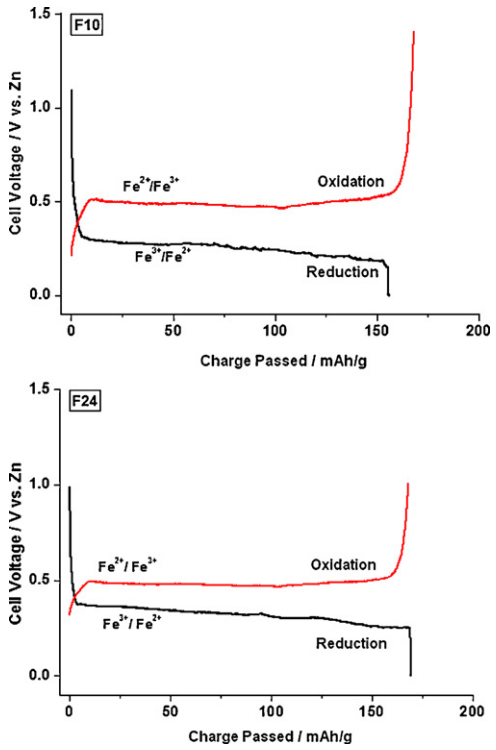

Fig. 5. Reduction/oxidation profiles of F10 and F24 with zinc as anode at a current density of 0.2 mA/cm^2. The cell contained saturated aqueous LiOH containing 1 mol/L of $ZnSO_4$ as electrolyte. The reduction process occurred prior to the oxidation process.

was more than +1.0 V. The reduction–oxidation profiles for F10 and F24 are shown in Fig. 5. The electrochemical characteristics for both samples show similar patterns. During the reduction process, there is an initial drop in voltage from +1.0 to +0.35 V, followed by a long plateau (at +0.33 V) corresponding to insertion of electrons and Li^+ ions into the α-Fe_2O_3 phase. The quantity of charge passed (170 mAh/g) corresponds to 1.04 mol of lithium inserted per mol of α-Fe_2O_3. During the subsequent oxidation process, the reaction appears reversible, delivering 160 mAh/g of charge for an efficiency of 94%. The storage capacity and coulombic efficiency of α-Fe_2O_3 microparticles observed in this study are comparable to previous reported studies [19,24] i.e. 250 mAh/g and 99% for non-aqueous lithium-ion batteries. The charge plateau at the cell voltage of +0.5 V corresponds to a reversal of the reduction reaction. The major difference between the F10 and F24 was the greater capacity (by *ca* 8%) of latter. This is consistent with the detection of higher α-Fe_2O_3 concentrations on the surface of F24 compared to F10 using the aforesaid XPS analysis. These preliminary studies show the intriguing behaviour of this α-Fe_2O_3 phase engineered into this micro-structure.

4. Conclusions

It has been demonstrated that mineralogically pure cubic α-Fe_2O_3 (hematite) microparticles can be synthesized via a simple one-pot hydrothermal reaction using glycine and ferric chloride as reactants. The reaction mechanism proposed in this study offers some fundamental understanding of the precipitation process in the reaction. Information presented here may aid to improve the design of microparticle synthetic processes in future studies. The application of these α-Fe_2O_3 microparticles should not be limited to the electrochemistry field and perhaps, future studies should include application in the biomedical field such as drug delivery.

Acknowledgment

The authors acknowledge the technical assistance provided by Martelle Chamberlain, Peter Fallon, Sue Farr, Stewart Kelly and Ken Seymour. M. Minakshi gratefully acknowledges financial support from an ARC Discovery Project (DP 1092543) from the Australian Research Council.

References

[1] X. Chen, Z. Zhang, Z. Qiu, C. Shi, X. Li, A facile biomolecule-assisted approach for fabricating α-Fe_2O_3 nanowires in solution, Solid State Commun. 140 (2006) 267–269.
[2] A.S. Teja, P.-Y. Koh, Synthesis, properties, and applications of magnetic iron oxide nanoparticles, Prog. Cryst. Growth Charact. Mater. 55 (2009) 22–45.
[3] M. Cao, T. Liu, S. Gao, G. Sun, X. Wu, C. Hu, L.W. Zhong, Single-crystal dendritic micro-pines of magnetic α-Fe_2O_3: large-scale synthesis, formation mechanism, and properties, Angew. Chem. Int. Ed. 44 (2005) 4197–4201.
[4] J. Chen, L. Xu, W. Li, X. Gou, α-Fe_2O_3 nanotubes in gas sensor and lithium-ion battery applications, Adv. Mater. 17 (2005) 582–586.
[5] X. Hu, J.C. Yu, J. Gong, Q. Li, G. Li, α-Fe_2O_3 nanorings prepared by a microwave-assisted hydrothermal process and their sensing properties, Adv. Mater. 19 (2007) 2324–2329.
[6] X. Liu, G. Qiu, A. Yan, Z. Wang, X. Li, Hydrothermal synthesis and characterization of α-FeOOH and α-Fe_2O_3 uniform nanocrystallines, J. Alloys Compd. 433 (2007) 216–220.
[7] H. Xu, X. Wang, L. Zhang, Selective preparation of nanorods and micro-octahedrons of Fe_2O_3 and their catalytic performances for thermal decomposition of ammonium perchlorate, Powder Technol. 185 (2008) 176–180.
[8] F. Song, J. Guan, X. Fan, G. Yan, Single-crystal star-like arrayed particles of hematite: synthesis, formation mechanism and magnetic properties, J. Alloys Compd. 485 (2009) 753–758.
[9] S. Zeng, K. Tang, T. Li, Z. Liang, D. Wang, Y. Wang, W. Zhou, Hematite hollow spindles and microspheres: selective synthesis, growth mechanisms, and application in lithium ion battery and water treatment, J. Phys. Chem. C 111 (2007) 10217–10225.
[10] X. Liu, H. Wang, C. Su, P. Zhang, J. Bai, Controlled fabrication and characterization of microspherical $FeCO_3$ and α-Fe_2O_3, J. Colloid Interface Sci. 351 (2010) 427–432.
[11] J.S. Chen, T. Zhu, X.H. Yang, H.G. Yang, X.W. Lou, Top-down fabrication of α-Fe_2O_3 single-crystal nanodiscs and microparticles with tunable porosity for largely improved lithium storage properties, J. Am. Chem. Soc. 132 (2010) 13162–13164.
[12] M. Tadić, N. Čitaković, M. Panjan, Z. Stojanović, D. Marković, V. Spasojević, Synthesis, morphology, microstructure and magnetic properties of hematite submicron particles, J. Alloys Compd. 509 (2011) 7639–7644.
[13] J.R. Lee, J. Lee, S.K. Kim, K.P. Kim, H.S. Park, W.-S. Yeo, Mass spectrometry signal amplification method for attomolar detection of antigens using small-molecule-tagged gold microparticles, Angew. Chem. 120 (2008) 9660–9663.
[14] H.S. Khare, D.L. Burris, A quantitative method for measuring nanocomposite dispersion, Polymer 51 (2010) 719–729.
[15] C. Su, H. Wang, X. Liu, Controllable fabrication and growth mechanism of hematite cubes, Cryst. Res. Technol. 46 (2011) 209–214.
[16] Z. Li, X. Lai, H. Wang, D. Mao, C. Xing, D. Wang, Direct hydrothermal synthesis of single-crystalline hematite nanorods assisted by 1,2-propanediamine, Nanotechnology 20 (2009) 245603.
[17] H. Singh, S. Bhagwat, S. Jouen, B. Lefez, A.A. Athawale, B. Hannoyer, S. Ogale, Elucidation of the role of hexamine and other precursors in the formation of magnetite nanorods and their stoichiometry, Phys. Chem. Chem. Phys. 12 (2010) 3246–3253.
[18] P.M. May, K. Murray, JESS, a joint expert speciation system-II. The thermodynamic database, Talanta 38 (1991) 1419–1426.
[19] G. Jain, M. Balasubramanian, J.J. Xu, Structural studies of lithium intercalation in a nanocrystalline α-Fe_2O_3 compound, Chem. Mater. 18 (2006) 423–434.
[20] Y. Han, Y. Wang, L. Li, Y. Wang, L. Jiao, H. Yuan, S. Liu, Preparation and electrochemical performance of flower-like hematite for lithium-ion batteries, Electrochim. Acta 56 (2011) 3175–3181.
[21] R. Ruffo, C. Wessells, R.A. Huggins, Y. Cui, Electrochemical behavior of $LiCoO_2$ as aqueous lithium-ion battery electrodes, Electrochem. Commun. 11 (2009) 247–249.
[22] M. Minakshi, D.R.G. Mitchell, The influence of bismuth oxide doping on the rechargeability of aqueous cells using MnO_2 cathode and LiOH electrolyte, Electrochim. Acta 53 (2008) 6323–6327.
[23] M. Minakshi, Rechargeable capacity increase of manganese dioxide batteries, PCT Int./WO2011/044644 A1 20110421.
[24] J.J. Xu, G. Jain, A nanocrystalline ferric oxide cathode for rechargeable lithium batteries, Electrochem. Solid State Lett. 6 (2003) A190–A193.